

# Effect of Postannealing on the Properties of a Ta-doped $\text{Li}_7\text{La}_3\text{Zr}_2\text{O}_{12}$ Solid Electrolyte Degraded by Li Dendrite Penetration

Ryoji Inada<sup>1,\*</sup>, Atsuto Takeda<sup>1</sup>, Yusuke Yamazaki<sup>1</sup>, Shotaro Miyake<sup>1</sup>, Yoji Sakurai<sup>1</sup>, Venkataraman Thangadurai<sup>2,\*</sup>

<sup>1</sup> Department of Electrical and Electronic Information Engineering, Toyohashi University of Technology, 1-1 Hibarigaoka, Tempaku-cho, Toyohashi, Aichi 441-8580, Japan.

<sup>2</sup> Department of Chemistry, University of Calgary, 2500 University Dr NW, Calgary, Alberta, T2N 1N4, Canada.

\*Corresponding authors:

R. I.: E-mail address: inada.ryoji.qr@tut.jp

V. T.: E-mail address: vthangad@ucalgary.ca

## Abstract

In this study, we investigated the effect of post annealing on the properties for garnet-type Ta-doped  $\text{Li}_{6.55}\text{La}_3\text{Zr}_{1.55}\text{Ta}_{0.45}\text{O}_{12}$  (Ta-LLZO) ceramic solid electrolyte degraded by lithium dendrite penetration during electrochemical Li plating and stripping testing in a Li/Ta-LLZO/Li symmetric cell. After the electrochemical testing in the symmetric cell, Ta-LLZO pellet was taken out of the cell and then annealed at 800 or 900°C for 4 h in air. It was confirmed that locally discolored spots on Ta-LLZO surface at which Li dendrite penetrated disappeared after the post annealing. The total conductivity of annealed Ta-LLZO pellet was lower than the initial one, but retained above  $10^{-4}$  S  $\text{cm}^{-1}$  at room temperature. When the soft-shortened or degraded area size by Li dendrite penetration is localized and smaller than the area size for Ta-LLZO, it is expected that the degradation of conductivity of annealed Ta-LLZO becomes smaller. Obtained electrochemical results indicates the possibility for reusing degraded garnet-type solid electrolyte by Li dendrite penetration in another all-solid-state Li battery.

**Keywords:** solid electrolyte, garnet, ionic conductivity, Li dendrite, post annealing

## 1. Introduction

Development of solid inorganic lithium-ion conducting materials for the use as solid electrolyte is indispensable for realization of next generation all-solid-state lithium (Li) batteries with high safety and reliability.<sup>1,2</sup> The materials used for solid electrolyte must have not only high ionic conductivity above  $10^{-3}$  S cm<sup>-1</sup> at room temperature but also chemical stabilities against Li metal, air and moisture. Although oxide based solid electrolyte materials have rather lower conductivity than sulfide based one, they have other advantages such as their chemical stability and handling.<sup>3</sup> Among the various oxide-based solid electrolyte materials, garnet-type oxide with the formula of Li<sub>7</sub>La<sub>3</sub>Zr<sub>2</sub>O<sub>12</sub> (LLZO) has attracted much attention because of the high conductivity at room temperature, excellent thermal performance, and high stability against Li metal.<sup>4-6</sup> Substitution of higher valence cation such as Nb<sup>5+</sup><sup>7-9</sup> and Ta<sup>5+</sup><sup>10-14</sup> into Zr<sup>4+</sup> site stabilizes cubic phases and enhances ionic conductivity to  $1 \times 10^{-3}$  S cm<sup>-1</sup> at room temperature, but the stability against a Li metal electrode for Ta-doped LLZO is much superior to Nb-doped one.<sup>15-17</sup>

Although the use of Li metal with large gravimetric theoretical capacity (= 3,860 mAh g<sup>-1</sup>) and the lowest redox potential as a negative electrode leads to high energy density of batteries, the formation of a solid-solid interface between LLZO and Li metal electrode is another challenging issue. Poor interfacial connection causes non-uniform Li plating and intergranular penetration of fibrous Li metal in polycrystalline LLZO when the cell is cycled particularly at low temperature and high current densities, resulting into internal short circuit failure.<sup>18-22</sup> Many efforts have been made to reduce the interfacial charge-transfer resistance between LLZO and Li and improve the stability against Li plating/stripping at the interface including the introduction of thin film layers,<sup>23-26</sup> eliminating the secondary phases by polishing or chemical etching the surface of LLZO and thermal treatment at specific temperatures before and/or after contacting with Li,<sup>20,27-30</sup> and controlling the microstructures of LLZO.<sup>31-38</sup> Precise analysis and understanding of the phenomenon occurring at the Li/LLZO interface can help to solve this issue.<sup>21,39-43</sup>

It is no doubt that the establishment of prevention technology for short circuit failures is a top priority issue for the development of all-solid-state batteries with Li metal as a negative electrode. On the other hand, from the viewpoint of effective use of material resources, it is worth considering the possibility of reusing LLZO extracted from a solid-state battery after a short circuit failure occurred. If the amount of fibrous Li metal propagating in LLZO is small and short circuit area is much localized, LLZO may be reused by removing the fibrous Li metal therein. In this work, we investigated the reusability of garnet-type

Ta-doped  $\text{Li}_{6.55}\text{La}_3\text{Zr}_{1.55}\text{Ta}_{0.45}\text{O}_{12}$  (Ta-LLZO) ceramic solid electrolyte shorted or degraded by Li metal penetration during electrochemical Li plating/stripping testing for a Li/Ta-LLZO/Li symmetric cell. Ta-LLZO was taken out of tested cell after the degradation occurred and then annealed in air. We confirmed that an annealed Ta-LLZO maintains the conductivity well above  $10^{-4} \text{ S cm}^{-1}$  at room temperature. If the area size of Ta-LLZO becomes larger and shorted area in Ta-LLZO is more localized, the degradation of the conductivity will be reduced and post-annealed Ta-LLZO after short circuit failure may be reusable as an electrolyte for another solid-state cell.

## 2. Experimental Section

Ta-LLZO ( $\text{Li}_{6.55}\text{La}_3\text{Zr}_{1.55}\text{Ta}_{0.45}\text{O}_{12}$ ) pellet samples were synthesized by a conventional solid state reaction method described in the literatures.<sup>20,45</sup> We used Pt-Au alloy crucible for sintering process at  $1150^\circ\text{C}$  and substitution level of  $\text{Ta}^{5+}$  to  $\text{Zr}^{4+}$  site was set to 0.45 for cubic phase stabilization with high conductivity. A diameter and a thickness of a finally obtained pellet is 0.9 cm and 0.16 cm. The relative density of the pellet (measured density normalized by the theoretical one) is approximately 93%. The crystal phase of the sample was identified by X-ray diffraction (XRD, Rigaku Multiflex) using  $\text{CuK}\alpha$  radiation, with measurement range  $2\theta = 5\text{--}90^\circ$  and step interval of  $0.02^\circ$ .

Before assembling a Li/Ta-LLZO/Li symmetric cell, both end surfaces of Ta-LLZO pellet were polished to remove surface contamination. Both the end surfaces of Ta-LLZO pellet was coated with Au films (thickness  $\sim 100 \text{ nm}$ ) by sputtering. Then, the pellet was sandwiched with two Li metal foils with diameter of 0.8 cm and thickness of 0.15 mm with a commercial cell fixture (Hosen, KP-Solid Cell) in argon-filled glove box and heated at  $175^\circ\text{C}$  for 5 hours,<sup>20,43</sup> to reduce the interfacial charge-transfer resistance ( $R_i$ ) between Ta-LLZO and Li via alloying reaction of Li and Au.<sup>23,26,35</sup> The symmetric cell was cycled at various current densities and the cell voltage response was measured using a Battery Test System (TOSCAT-3100, TOYO SYSTEM) at  $25^\circ\text{C}$  until the cell showed an evidence of Li dendrite penetration in Ta-LLZO. Electrochemical impedance spectroscopy (EIS) measurement was carried out in a frequency range from 4 to  $8 \times 10^6 \text{ Hz}$  with an impedance meter (HIOKI, IM3536) before and after the cycling tests to characterize the cell impedance.

After the electrochemical testing, the symmetric cell was disassembled and the degraded Ta-LLZO pellet was taken out. Residues containing Li metal and its reaction product with Au on the pellet surface

were removed by ethanol and light polishing. Then, the pellet was annealed at 900°C for 4h in air. Both the end surfaces of annealed Ta-LLZO pellet were coated by Au films and evaluated the ionic conductivity by EIS measurements. XRD measurement on the surface of annealed Ta-LLZO after galvanostatic testing were also carried out for checking the presence of secondary phases. Field emission scanning electron microscope (FE-SEM, Hitachi High-Technologies, SU8000 Type II) was used to investigate the microstructure of fractured cross-sectional surface for annealed pellet after the galvanostatic testing. One of annealed Ta-LLZO pellets was used for the second galvanostatic testing at 25°C in a symmetric cell with Li metal electrodes to confirm if it can still perform well in a solid-state Li battery after the annealing treatment in air.

### 3. Results and discussion

The left graphs for Figure 1 show the voltage response for three Li/Ta-LLZO/Li symmetric cells composed of Li metal electrodes and Ta-LLZO pellet in galvanostatic testing at 25°C. The details for assembling the cell are described in experimental section. For cell A, the initial value of current density was set to 0.02 mA cm<sup>-2</sup> and increased by 0.02 mA cm<sup>-2</sup> per cycle. While for cell B and cell C, the initial value of current density was 0.05 mA cm<sup>-2</sup>, which was increased by 0.05 mA cm<sup>-2</sup> every five cycles. As can be seen, voltage drops are increased gradually with increasing the current densities applied to the symmetric cell, but the sudden drops and fluctuation of cell voltages occur at current densities of 0.3–0.4 mA cm<sup>-2</sup>, indicating that potential Li dendrites penetrate and propagate into Ta-LLZO solid electrolyte at this point.

The Nyquist plot of electrochemical impedance for each symmetric cell at 27°C is also shown in the right graphs for Figure 1. Here,  $Z'$  and  $Z''$  represent the real and imaginary parts for impedance. Before the galvanostatic testing, the plot for each symmetric cell is composed of a large semicircle with a characteristic frequency of 2.5–4 MHz and a small distorted one at low frequency range. The contribution of ionic conduction for sintered Ta-LLZO was obtained from the high frequency impedance data (0.2–0.3 MHz).<sup>20,35,44</sup> The areal resistance of Ta-LLZO pellet in each tested cell is found to be 160–180 Ω cm<sup>2</sup>. Taking into account the pellet thickness (= 0.16 cm), the conductivity of Ta-LLZO pellets is estimated to be 0.89–1.0 mS cm<sup>-1</sup>, which agree well with the data reported in our previous works.<sup>20,35,44</sup> Interfacial charge transfer resistance  $R_{\text{int}}$  for cell A seems to be larger than others but the value is approximately 15 Ω cm<sup>2</sup>. For the cell B and cell C, it is considered that the contribution for interface charge transfer between Li metal

is partly contained in a large semicircle. Using  $Z'$  data below 0.25 MHz,  $R_{\text{int}}$  for cell B and cell C is estimated to be  $13 \Omega \text{ cm}^2$  and  $7 \Omega \text{ cm}^2$ , respectively. The difference in  $R_{\text{int}}$  among the tested cells may be caused by the variations in polished surface microstructure on the pellets before attached Li. After the galvanostatic testing, the cell impedance are reduced to  $49 \Omega \text{ cm}^2$  for cell A,  $16 \Omega \text{ cm}^2$  for cell B and  $74 \Omega \text{ cm}^2$  for cell C. It is worth noting that the plots in cell A and cell C are shaped like part of a semicircle, but the plots in cell B are concentrated at one point on the  $Z'$  axis. These results clearly indicate that cell A and cell C are not shorted while cell B is shorted completely by Li dendrite propagation. Reduction in the size of semicircles for cell A and cell C after galvanostatic testing may be attributed to the reduced effective thickness between two Li metal electrodes and/or increase in the effective electrode area due to Li dendrite penetration in Ta-LLZO.

After the galvanostatic testing, shorted and/or degraded Ta-LLZO pellets were taken out from each symmetric cell and then annealed at  $800^\circ\text{C}$  or  $900^\circ\text{C}$  for 4 hours in air. Figure 2 shows the exterior photos Ta-LLZO pellets before and after galvanostatic testing taken out from three symmetric cells. Before annealing, it is clearly confirmed that some areas on the pellet surface have turned dark gray or black with the penetration of Li dendrites. Compared with the pellets tested in cell A and cell C, the pellet tested in cell B has many discolored spots/areas on the pellet surface, suggesting that Li dendrite penetration occurred in many areas. It is difficult to control the area size of Li dendrite propagation into Ta-LLZO in our experiment and well understood why the propagation of Li dendrites in Ta-LLZO tested in cell B differed so much from others. After the post annealing, these dark gray or black areas turned to white but slightly different from original color of Ta-LLZO. Only for the pellet tested in cell B, the discoloration to white appears uniform over the entire surface of the pellet.

X-ray diffraction patterns measured on the surface for as-prepared Ta-LLZO pellet and annealed ones after galvanostatic testing are compared in Figure 3. As-prepared Ta-LLZO pellet and the annealed one tested in cell A have cubic garnet phases and other secondary phases are hardly confirmed. Comparing with the calculated pattern for cubic  $\text{Li}_7\text{La}_3\text{Zr}_2\text{O}_{12}$ , all the peaks from Ta-LLZO are shifted toward a higher angle. This is attributed to the reduction of lattice size by substitution of  $\text{Zr}^{4+}$  (72 pm) by smaller  $\text{Ta}^{5+}$  (64 pm).<sup>10-14</sup> For the pellet tested in cell B and annealed at  $900^\circ\text{C}$ , not only the peaks from cubic garnet phase but also the weak peaks from  $\text{La}_2\text{O}_3$  (PDF No. 00-054-0123) phase and strong peaks from  $\text{La}_2\text{Zr}_2\text{O}_7$  (PDF No. 01-075-0346) and  $\text{La}_3\text{TaO}_7$  (PDF No. 00-038-1418) phases were detected. These secondary phases are

considered to be formed by Li loss from Ta-LLZO during post annealing.<sup>4</sup> For the pellet tested in cell C and annealed at 800°C, small 002 peak from Li<sub>2</sub>CO<sub>3</sub> (PDF No. 00-022-1141) was detected at  $2\theta = 31\text{--}32^\circ$ , together with the peaks from cubic garnet phase. The formation of La<sub>2</sub>O<sub>3</sub>, La<sub>2</sub>Zr<sub>2</sub>O<sub>7</sub> and La<sub>3</sub>TaO<sub>7</sub> phases was observed only in the pellet tested in cell B and not confirmed in the pellet tested in cell A annealed at same temperature (= 900°C). Therefore, the formation of impurity phases mentioned above may be related to the size of the Li dendrite penetration area rather than the annealing temperature. In our experiment, Li metal foils attached onto Ta-LLZO pellet is removed using ethanol after the galvanostatic testing. During the treatment with ethanol, Li dendrites that have penetrated near the pellet end surface are removed together with the Li foil and then the micro-sized pores and cracks are formed. Since the Li dendrite penetration area on the pellet tested in cell B is much wider than others (Figure 2), it can be speculated that these pores and cracks are formed in a wider area than in others tested in cell A and cell C. Consequently, excess Li loss from Ta-LLZO grains and the formation of impurity phases such as La<sub>2</sub>O<sub>3</sub>, La<sub>2</sub>Zr<sub>2</sub>O<sub>7</sub> and La<sub>3</sub>TaO<sub>7</sub> easily occur near the end-surface of pellet tested in cell B.

Figure 4 shows the Nyquist plots for electrochemical impedance for as-prepared Ta-LLZO and annealed Sample A (cell A) and Sample C (cell C) after galvanostatic testing. For the measurements, ionic blocking Au electrodes are deposited on both end surfaces of each pellet by sputtering. For as-prepared Ta-LLZO (Figure 4a), the plot at room temperature is composed of a linear tail at frequency below 0.2 MHz and a small part of the semicircle at frequency higher than 0.2 MHz. It is considered that the intersection of the exterior straight line of the data in the linear tail and the  $Z'$  axis corresponds to the total resistance of the pellet. As results, the total ionic conductivity  $\sigma_{\text{total}}$  for as-prepared Ta-LLZO is estimated to be 1 mS cm<sup>-1</sup> at 27°C and 3.1 mS cm<sup>-1</sup> at 52°C, respectively. For annealed Ta-LLZO pellet tested in cell A (Figure 4b), it is confirmed a small semicircle at frequency range from 3 kHz to 1 MHz, which was not observed in as-prepared sample. The frequency range in which the semicircle was observed corresponds well with the frequency range for the ionic conduction at grain-boundary.<sup>4</sup> Estimating the apparent total resistance from the intersection of the right end of this semicircle and the  $Z'$  axis,  $\sigma_{\text{total}}$  for annealed Ta-LLZO tested in cell A is calculated to 0.67 mS cm<sup>-1</sup> at 27°C and 1.6 mS cm<sup>-1</sup> at 52°C. For annealed Ta-LLZO pellet tested in cell C (Figure 4d), the plot is similar as the sample tested in cell A and  $\sigma_{\text{total}}$  is calculated to 0.55 mS cm<sup>-1</sup> at 27°C and 2.2 mS cm<sup>-1</sup> at 52°C.

On the other hand, the plot for annealed Ta-LLZO tested in cell B contains a large distorted semicircle

at frequency range from 7 kHz to 1.3 MHz at 27°C (Figure 4c). Although the semicircle is tilted on the complex  $Z''-Z'$  plane and it is slightly difficult to distinguish between the linear tail in the low frequency range and the left edge of the semicircle, apparent total resistance is expected to be from 3000 to 4000  $\Omega$  cm. Consequently,  $\sigma_{\text{total}}$  at 27°C for annealed Ta-LLZO tested in cell B is expected to be approximately 0.25–0.3  $\text{mS cm}^{-1}$  and much lower than others. At 52°C, the observation of tilted semicircle in measured impedance data becomes very difficult. In annealed Ta-LLZO tested in cell B, Li dendrites were formed and propagated in the widest area during the galvanostatic testing of a symmetric cell (see Figure 2), and many secondary phases were formed by the post annealing (see Figure 3). The reaction products such as  $\text{La}_2\text{O}_3$ ,  $\text{La}_2\text{Zr}_2\text{O}_7$  and  $\text{La}_3\text{TaO}_7$  formed by post annealing become obstacles for Li ion conduction.

In Figure 5, the temperature dependence of as-prepared Ta-LLZO pellet and annealed ones after tested in cell A and cell C is compared. Activation energy  $E_a$  for  $\sigma_{\text{total}}$ , which is closely related to the slope of conductivity data in Figure 5, was estimated to be 0.39 eV for as-prepared Ta-LLZO, 0.37 eV for annealed one tested in cell A and 0.42 eV for annealed one tested in cell C, respectively.  $E_a$  for annealed Ta-LLZO tested in cell C is slightly higher than the one tested in cell A, which may be influenced by the amounts of secondary phase formed by post annealing and slightly larger contribution of grain-boundary resistance (Figure 4b and 4d). It is noted that the estimation of  $E_a$  for annealed Ta-LLZO tested in cell B was difficult because the accurate evaluation of  $\sigma_{\text{total}}$  is difficult from the impedance data. Hence,  $\sigma_{\text{total}}$  data for this sample is not plotted in Figure 5.

For further discussion, we observed the microstructures of the fractured cross sectional surface of annealed Ta-LLZO pellets tested in cell B and cell C by FE-SEM and the results are summarized in Figure 6. At the region near the center of cross section, the microstructure for both samples is not so different and dense polycrystalline structure composed of Ta-LLZO grains with the size of 5–10  $\mu\text{m}$  is confirmed clearly, which is consistent with the microstructure of as-prepared Ta-LLZO reported in our previous work.<sup>20,44</sup> However, the microstructure near the end face that was in contact with a Li metal electrode in a symmetric cell is significantly different among the samples. For annealed Ta-LLZO tested in cell B (Figure 6a), in addition to the fact that the structure that seems to be Ta-LLZO grains can hardly be observed, many finely crushed particles can be seen in the region from the end surface to 5  $\mu\text{m}$ . Such a large structural change is related to the formation of  $\text{La}_2\text{O}_3$ ,  $\text{La}_2\text{Zr}_2\text{O}_7$  and  $\text{La}_3\text{TaO}_7$  phases. These results suggest that the ionic conducting property in this sample is not uniform along a thickness direction of the pellet and not degraded

remarkably near the center part of cross section. On the other hand, together with the fine particles with the size of 1–3  $\mu\text{m}$ , we can confirm Ta-LLZO grains near the end surface in annealed Ta-LLZO tested in cell C (Figure 6b). The structural change near the end surface for this sample seems to be much smaller than the one tested in cell B, resulting into the limited degradation of ionic conducting property shown in Figure 4d and 5.

Lastly, the results for the second galvanostatic testing at 25°C for the symmetric Li cell composed of annealed Ta-LLZO pellet tested in cell A are shown in Figure 7(a). As can be seen, the cell is stable cycled at current density of 0.18  $\text{mA cm}^{-2}$  but the sudden drop of cell voltage at 0.2  $\text{mA cm}^{-2}$  where Li dendrite penetration into annealed Ta-LLZO occurred. Although the tolerance for Li dendrite penetration seems to be degraded slightly, Li plating and stripping can be performed on annealed Ta-LLZO. Structural changes near the end surfaces ~~near the end face~~ of pellet (Figure 6(b)) and impurity phases formed by post annealing may contribute to the ease of Li dendrite penetration, but it is necessary to increase the number of samples and examine them in detail in the future. Figure 7(b) shows the Nyquist plots of electrochemical impedance at 27°C for the symmetric cell with annealed Ta-LLZO before and after galvanostatic testing. Comparing to the first testing (Figure 1(a)), the distorted semicircle at frequency below 0.2 MHz becomes larger, which is due to the increase in grain-boundary resistance for annealed Ta-LLZO (Figure 4(b)). The contribution of  $R_{\text{int}}$  between annealed Ta-LLZO and a Li metal electrode may be also contained here and similar as the first testing with as-prepared Ta-LLZO. After the galvanostatic testing, the residual cell impedance is confirmed to be 100  $\Omega \text{ cm}^2$  and the plot shaped like part of a semicircle, which indicates that the cell with annealed Ta-LLZO is not shorted.

#### 4. Conclusion

In conclusion, we investigated the effect of post annealing on the properties for Ta-LLZO solid electrolytes degraded by Li dendrite penetration during electrochemical Li plating and stripping testing. After the galvanostatic testing in the symmetric cell, Ta-LLZO pellet was taken out of the cell and then annealed at 800 or 900°C in air. Locally discolored spots on Ta-LLZO surface at which Li dendrite penetrated turned to white after the post annealing. The total conductivity of annealed Ta-LLZO pellet was lower than the initial one, but retained well above  $10^{-4} \text{ S cm}^{-1}$  at room temperature. The decrease in total conductivity for annealed Ta-LLZO is mainly attributed to the formation of impurity phases and structural

change near the end surface of pellets, and the degree of degradation depends on the area size for Li dendrite penetration. Moreover, although the tolerance for Li dendrite penetration could be degraded in annealed Ta-LLZO, the Li plating and stripping in a symmetric cell with annealed Ta-LLZO can be performed. When the size of shorted or degraded area by Li dendrite penetration is localized and much smaller than the area size for Ta-LLZO, it is expected that the degradation of conductivity of annealed Ta-LLZO becomes smaller. Obtained results can be used as the basic data for reuse of degraded garnet-type solid electrolyte.

### Acknowledgements

This work was partly supported by Grant-in-Aid for Scientific Research (JSPS KAKENHI) Grant Number 16KK0127 and 19H02128 from the Japan Society for the promotion of Science (JSPS). We acknowledged the support of the Cooperative Research Facility Center at Toyohashi University of Technology. R. I. also thanks the University of Calgary for the visiting Associate Professorship that has been funded by JSPS KAKENHI Number 16KK0127.

### References

- (1) Zheng, F.; Kotobuki, M.; Song, S.; Lei, M.O.; Lu, L. Review on solid electrolytes for all-solid-state lithium-ion batteries. *J. Power Sources* **2018**, *389*, 198–213.
- (2) Takada, K. Progress in solid electrolytes toward realizing solid-state lithium batteries. *J. Power Sources* **2018**, *394*, 74–85.
- (3) Ren, Y.; Chen, K.; Chen, R.; Liu, T.; Zhang, Y.; Nan, C. Oxide electrolytes for lithium batteries. *J. Ame. Ceram. Soc.* **2015**, *98*, 3603–3623.
- (4) Murugan, R.; Thangadurai, V.; Weppner, W. Fast lithium ion conduction in garnet-type  $\text{Li}_7\text{La}_3\text{Zr}_2\text{O}_{12}$ . *Angew. Chem. Int. Ed.* **2007**, *46*, 7778–7781.
- (5) Samson, A.J.; Hofstetter, K.; Bag, S.; Thangadurai, V. A bird's-eye view of Li-stuffed garnet-type  $\text{Li}_7\text{La}_3\text{Zr}_2\text{O}_{12}$  ceramic electrolytes for advanced all-solid-state Li batteries. *Energy Environ. Sci.* **2019**, *12*, 2957–2975.
- (6) Wang, C.; Fu, K.; Palakkathodi Kammampata, S.; McOwen, D.W.; Zhang, L.; Hitz, G.T.; Nolan, A.; Samson, A.; Wachsman, E.D.; Mo, Y.; Thangadurai, V.; Hu, L. Garnet-type solid-state electrolytes: materials, interfaces, and batteries. *Chem. Rev.* **2020**, *120*, 4257–4300

- (7) Ohta, S.; Kobayashi T.; Asaoka, T. High lithium ionic conductivity in the garnet-type oxide  $\text{Li}_{7-x}\text{La}_3(\text{Zr}_{2-x}\text{Nb}_x)\text{O}_{12}$  ( $X = 0-2$ ). *J. Power Sources* **2011**, *196*, 3342–3345.
- (8) Kihira, Y.; Ohta, S.; Imagawa, H.; Asaoka, T. Effect of simultaneous substitution of alkali earth metals and Nb in  $\text{Li}_7\text{La}_3\text{Zr}_2\text{O}_{12}$  on lithium-ion conductivity. *ECS Electrochem. Lett.* **2013**, *2*, A56–A59.
- (9) Kataoka, K.; Nagata, H.; Akimoto, J. Lithium-ion conducting oxide single crystal as solid electrolyte for advanced lithium battery application. *Sci. Rep.* **2018**, *8*, 9965.
- (10) Li, Y.; Han, J.-T.; Wang, C.-A.; Xie, H.; Goodenough, J.B. Optimizing  $\text{Li}^+$  conductivity in a garnet framework. *J. Mater. Chem.* **2012**, *22*, 15357–15361.
- (11) Wang, Y.; Wei, L. High ionic conductivity lithium garnet oxides of  $\text{Li}_{7-x}\text{La}_3\text{Zr}_{2-x}\text{Ta}_x\text{O}_{12}$  compositions. *Electrochem. Solid State Lett.* **2012**, *15*, A68–A71.
- (12) Inada, R.; Kusakabe, K.; Tanaka, T.; Kudo, S.; Sakurai, Y. Synthesis and properties of Al-free  $\text{Li}_{7-x}\text{La}_3\text{Zr}_{2-x}\text{Ta}_x\text{O}_{12}$  garnet related oxides. *Solid State Ion.* **2014**, *262*, 568–572.
- (13) Inada, R.; Yasuda, S.; Tojo, M.; Tsuritani, K.; Tojo, T.; Sakurai, Y. Development of lithium-stuffed garnet-type oxide solid electrolytes with high ionic conductivity for application to all-solid-state batteries. *Front. Energy Res.* **2016**, *4*, 28.
- (14) Kataoka, K. Akimoto, J. High ionic conductor member of garnet-type oxide  $\text{Li}_{6.5}\text{La}_3\text{Zr}_{1.5}\text{Ta}_{0.5}\text{O}_{12}$ . *ChemElectroChem* **2018**, *5*, 2551–2557.
- (15) Nemori, H.; Matsuda, Y.; Mitsuoka, S.; Matsui, M.; Yamamoto, O.; Takeda, Y.; Imanishi, N. Stability of garnet-type solid electrolyte  $\text{Li}_x\text{La}_3\text{A}_{2-y}\text{B}_y\text{O}_{12}$  ( $A = \text{Nb}$  or  $\text{Ta}$ ,  $B = \text{Sc}$  or  $\text{Zr}$ ). *Solid State Ion.* **2015**, *282*, 7–12.
- (16) Kim, Y.; Yoo, A.; Schmidt, R.; Sharafi, A.; Lee, H.; Wolfenstine, J.; Sakamoto, J. Electrochemical Stability of  $\text{Li}_{6.5}\text{La}_3\text{Zr}_{1.5}\text{M}_{0.5}\text{O}_{12}$  ( $M = \text{Nb}$  or  $\text{Ta}$ ) against Metallic Lithium. *Front. Energy Res.* **2016**, *4*, 20.
- (17) Zhu, Y.; Connell, J.G.; Tepavcevic, S.; Zapol, P.; Garcia-Mendez, R.; Taylor, N.J.; Sakamoto, J.; Ingram, B.J.; Curtiss, L.A.; Freeland, J.W.; Fong D.D.; Markovic, N.M. Dopant-dependent stability of garnet solid electrolyte interfaces with lithium metal. *Adv. Energ. Mater.* **2019**, *9*, 1803440.
- (18) Ren, Y.; Shen, Y.; Lin, Y.; Nan, C.-W. Direct observation of lithium dendrites inside garnet-type lithium-ion solid electrolyte. *Electrochem. Commun.* **2015**, *57*, 27–30.

- (19) Cheng, E.J.; Sharafi, A.; Sakamoto, J. Intergranular Li metal propagation through polycrystalline  $\text{Li}_{6.25}\text{Al}_{0.25}\text{La}_3\text{Zr}_2\text{O}_{12}$  ceramic electrolyte. *Electrochim. Acta* **2017**, *223*, 85–91.
- (20) Inada, R.; Yasuda, S.; Hosokawa, H. Saito, M.; Tojo, T.; Sakurai, Y. Formation and stability of interface between garnet-type Ta-doped  $\text{Li}_7\text{La}_3\text{Zr}_2\text{O}_{12}$  solid electrolyte and lithium metal electrode. *Batteries* **2018**, *4*, 26.
- (21) Kazyak, E.; Garcia-Mendez, R.; LePage, W.S.; Sharafi, A.; Davis, A.L.; Sanchez, A.J.; Chen, K-H.; Haslam, C.; Sakamoto, J.; Dasgupta N.P. Li penetration in ceramic solid electrolytes: operando microscopy analysis of morphology, propagation, and reversibility. *Matter* **2020**, *2*, 1025–1048.
- (22) Cao, D.; Sun, X.; Li, Q.; Natan, A.; Xiang, P.; Zhu, H. Lithium dendrite in all-solid-state batteries: growth mechanisms, suppression strategies, and characterizations. *Matter* **2020**, *3*, 57–94.
- (23) Tsai, C.-L.; Roddatis, V.; Chandran, C.V.; Ma, Q.; Uhlenbruck, S.; Bram, M.; Heitjans, P.; Guillon, O.  $\text{Li}_7\text{La}_3\text{Zr}_2\text{O}_{12}$  interface modification for Li dendrite prevention. *ACS Appl. Mater. Interfaces* **2016**, *8*, 10617–10626.
- (24) Han, X.; Gong, Y.; Fu, K.; He, X.; Hitz, G.T.; Dai, J.; Pearse, A.; Liu, B.; Wang, H.; Rublo, G.; Mo, Y.; Thangadurai, V.; Wachsman E.D.; Hu, L. Negating interfacial impedance in garnet-based solid-state Li metal batteries. *Nat. Mater.* **2017**, *16*, 572–579.
- (25) Zhou, C.; Samson, A.J.; Hofstetter K.; Thangadurai V. A surfactant-assisted strategy to tailor Li-ion charge transfer interfacial resistance for scalable all-solid-state Li batteries. *Sustainable Energ. Fuels* **2018**, *2*, 2165–2170.
- (26) Huang, X.; Lu, Y.; Guo, H.; Song, Z.; Xiu, T.; Badding, M.E.; Wen, Z. None-mother-powder method to prepare dense Li-garnet solid electrolytes with high critical current density. *ACS Appl. Energy Mater.* **2018**, *1*, 5355–5365.
- (27) Sharafi, A.; Kazyak, E.; Davis, A.L.; Yu, S.; Thompson, T.; Siegel, D.J.; Dasgupta, N.P.; Sakamoto, J. Surface chemistry mechanism of ultra-low interfacial resistance in the solid-state electrolyte  $\text{Li}_7\text{La}_3\text{Zr}_2\text{O}_{12}$ . *Chem. Mater.* **2017**, *29*, 7961–7968.
- (28) Basappa, R.H.; Ito, T.; Yamada, H. Contact between garnet-type solid electrolyte and lithium metal anode: Influence on charge transfer resistance and short circuit prevention. *J. Electrochem. Soc.* **2017**, *164*, A666–A671.
- (29) Taylor, N.J.; Stangeland-Molo, S.; Haslam, C.G.; Sharafi, A.; Thompson, T.; Wang, M. Garcia-

- Mendez, R.; Sakamoto, J. Demonstration of high current densities and extended cycling in the garnet  $\text{Li}_7\text{La}_3\text{Zr}_2\text{O}_{12}$  solid electrolyte. *J. Power Sources* 2018, **396**, 314–318.
- (30) Motoyama, M.; Tanaka, Y.; Yamamoto, T.; Tsuchimine, N.; Kobayashi S.; Iriyama, Y. The Active interface of Ta-doped  $\text{Li}_7\text{La}_3\text{Zr}_2\text{O}_{12}$  for Li plating/stripping revealed by acid aqueous etching. *ACS Appl. Energ. Mater.* **2019**, *2*, 6720–6731.
- (31) Cheng, L.; Chen, W.; Kunz, M.; Persson, K.; Tamura, N.; Chen, G.; Doeff, M. Effect of surface microstructure on electrochemical performance of garnet solid electrolytes. *ACS Appl. Mater. Interfaces* **2015**, *7*, 2073–2081.
- (32) Sharafi, A.; Meyer, H.M.; Nanda, J.; Wolfenstine, J.; Sakamoto, J. Controlling and correlating the effect of grain size with the mechanical and electrochemical properties of  $\text{Li}_7\text{La}_3\text{Zr}_2\text{O}_{12}$  solid-state electrolyte. *J. Mater. Chem. A* **2017**, *5*, 21491–21504.
- (33) Basappa, R.H.; Ito, T.; Morimura, T.; Bekarevich, R.; Mitsuishi, K.; Yamada, H. Grain boundary modification to suppress lithium penetration through garnet-type solid electrolyte. *J. Power Sources* **2017**, *363*, 145–152.
- (34) Xu, B.; Li, W.; Duan, H.; Wang, H.; Guo, Y.; Li, H.; Liu, H.  $\text{Li}_3\text{PO}_4$ -added garnet-type  $\text{Li}_{6.5}\text{La}_3\text{Zr}_{1.5}\text{Ta}_{0.5}\text{O}_{12}$  for Li-dendrite suppression. *J. Power Sources* **2017**, *354*, 68–73.
- (35) Hosokawa, H.; Takeda, A.; Inada, R.; Sakurai, Y. Tolerance for Li dendrite penetration in Ta-doped  $\text{Li}_7\text{La}_3\text{Zr}_2\text{O}_{12}$  solid electrolytes sintered with  $\text{Li}_{2.3}\text{C}_{0.7}\text{B}_{0.3}\text{O}_3$  additive. *Mater. Lett.* **2020**, *279*, 128481.
- (36) Hitz, G.T.; McOwen, D.M.; Zhang, L.; Ma, Z.; Fu, Z.; Wen, Y.; Gong, Y.; Dai, J.; Hamann, T.R.; Hu, L.; Wachsman, E.D. High-rate lithium cycling in a scalable trilayer Li-garnet-electrolyte architecture. *Mater. Today* **2019**, *22*, 50–57.
- (37) Huo, H.; Liang, J.; Zhao, N.; Li, X.; Lin, X.; Zhao, Y.; Adair, K.; Li, R.; Guo, X.; Sun, X. Dynamics of the garnet/Li interface for dendrite-free solid-state batteries. *ACS Energy Lett.* **2020**, *5*, 2156–2164.
- (38) Song, S.; Wu, Y.; Dong, Z.; Deng, F.; Tang, W.; Yao, J.; Wen, Z.; Lu, L.; Hu, N.; Molenda, J. Multi-substituted garnet-type electrolytes for solid-state lithium batteries. *Ceram. Internat.* **2019**, *46*, 5489–5494.
- (39) Kim, J.-S.; Kim, H.; Badding, M.; Song, Z.; Kim, K.; Kim, Y.; Yun, D.-J.; Lee, D.; Chang, J.; Kim, S.; Im, D.; Park, S.; Kim, S.H.; Heo, S. Origin of intergranular Li metal propagation in garnet-based solid electrolyte by direct electronic structure analysis and performance improvement by bandgap

- engineering. *J. Mater. Chem. A* **2020**, *8*, 16892–16901.
- (40) Koshikawa, H.; Matsuda, S.; Kamiya, K.; Miyayama, M.; Kubo, Y.; Uosaki, K.; Hashimoto K. Nakanishi, S. Electrochemical impedance analysis of the Li/Au-Li<sub>7</sub>La<sub>3</sub>Zr<sub>2</sub>O<sub>12</sub> interface during Li dissolution/deposition cycles: Effect of pre-coating Li<sub>7</sub>La<sub>3</sub>Zr<sub>2</sub>O<sub>12</sub> with Au. *J. Electroanal. Chem.* **2019**, *835*, 143–149.
- (41) Wang, M.; Wolfenstine J.; Sakamoto, J. Temperature dependent flux balance of the Li/Li<sub>7</sub>La<sub>3</sub>Zr<sub>2</sub>O<sub>12</sub> interface. *Electrochim. Acta* **2019**, *296*, 842–847.
- (42) Wang, M.; Choudhury, R.; Sakamoto, J. Characterizing the Li-solid-electrolyte interface dynamics as a function of stack pressure and current density. *Joule* **2019**, *3*, 2165–2178.
- (43) Krauskopf, T.; Mogwitz, B. Hartmann, H. Singh, D.K.; Zeier, W.G.; Janek, J. The fast charge transfer kinetics of the lithium metal anode on the garnet-type solid electrolyte Li<sub>6.25</sub>Al<sub>0.25</sub>La<sub>3</sub>Zr<sub>2</sub>O<sub>12</sub>. *Adv. Energy Mater.* **2020**, *10*, 2000945.
- ~~(44) Awaka, J.; Takashima, A.; Kataoka, K.; Kijima, N.; Idemoto, Y.; Akimoto, J. Crystal structure of fast lithium ion conducting cubic Li<sub>7</sub>La<sub>3</sub>Zr<sub>2</sub>O<sub>12</sub>. *Chem. Lett.* **2011**, *40*, 60–62.~~
- (45) Inada, R.; Okuno,; T. Kito,; S. Tojo,; T. Sakurai, Y. Properties of lithium trivanadate film electrodes formed on garnet-type oxide solid electrolyte by aerosol deposition. *Materials* **2018**, *11*, 1570.

## Figure captions

**Figure 1.** Voltage response for galvanostatic testing and Nyquist plots (left) for electrochemical impedance for three Li/Ta-LLZO/Li symmetric cells (right) at room temperature: (a) cell A, (b) cell B and (c) cell C.

**Figure 2.** Photos of Ta-LLZO pellets before after galvanostatic testing taken out from each symmetric cell. The pellets before or after post annealing are shown in top or bottom image. Annealing temperatures are 900°C for the pellets tested in cell A and cell B and 800°C for the pellet tested in cell C.

**Figure 3.** XRD patterns of as-prepared Ta-LLZO pellet and post annealed at 800°C or 900°C for 4 hours in air after galvanostatic testing. Calculated or reported diffraction patterns for cubic  $\text{Li}_7\text{La}_3\text{Zr}_2\text{O}_{12}$ ,  $\text{Li}_2\text{CO}_3$  (PDF No. 00-022-1141),  $\text{La}_2\text{O}_3$  (PDF No. 00-054-0123),  $\text{La}_2\text{Zr}_2\text{O}_7$  (PDF No. 01-075-0346) and  $\text{La}_3\text{TaO}_7$  (PDF No. 00-038-1418) phases are shown as the references. The pellet tested in cell B shows impurity phases such as  $\text{La}_2\text{O}_3$ ,  $\text{La}_2\text{Zr}_2\text{O}_7$  and  $\text{La}_3\text{TaO}_7$ .

**Figure 4.** Nyquist plots for electrochemical impedance of Ta-LLZO pellets with Au ionic blocking electrodes: (a) as-prepared (before galvanostatic testing), (b) annealed at 900°C after tested in cell A, (c) annealed at 900°C after tested in cell B and (d) annealed at 800°C after tested in cell C.

**Figure 5.** Temperature dependence for total conductivity  $\sigma_{\text{total}}$  for as-prepared Ta-LLZO pellet and annealed ones after galvanostatic testing.

**Figure 6.** SEM images for fractured cross sectional surfaces for annealed Ta-LLZO pellets: (a) tested in cell B and (b) tested in cell C. Schematic illustration for observation areas by SEM is shown in (c).

**Figure 7.** (a) Voltage response for the second galvanostatic testing and (b) Nyquist plots for electrochemical impedance for a Li/annealed Ta-LLZO/Li symmetric cell at room temperature. We used annealed Ta-LLZO firstly tested in cell A for the measurement.

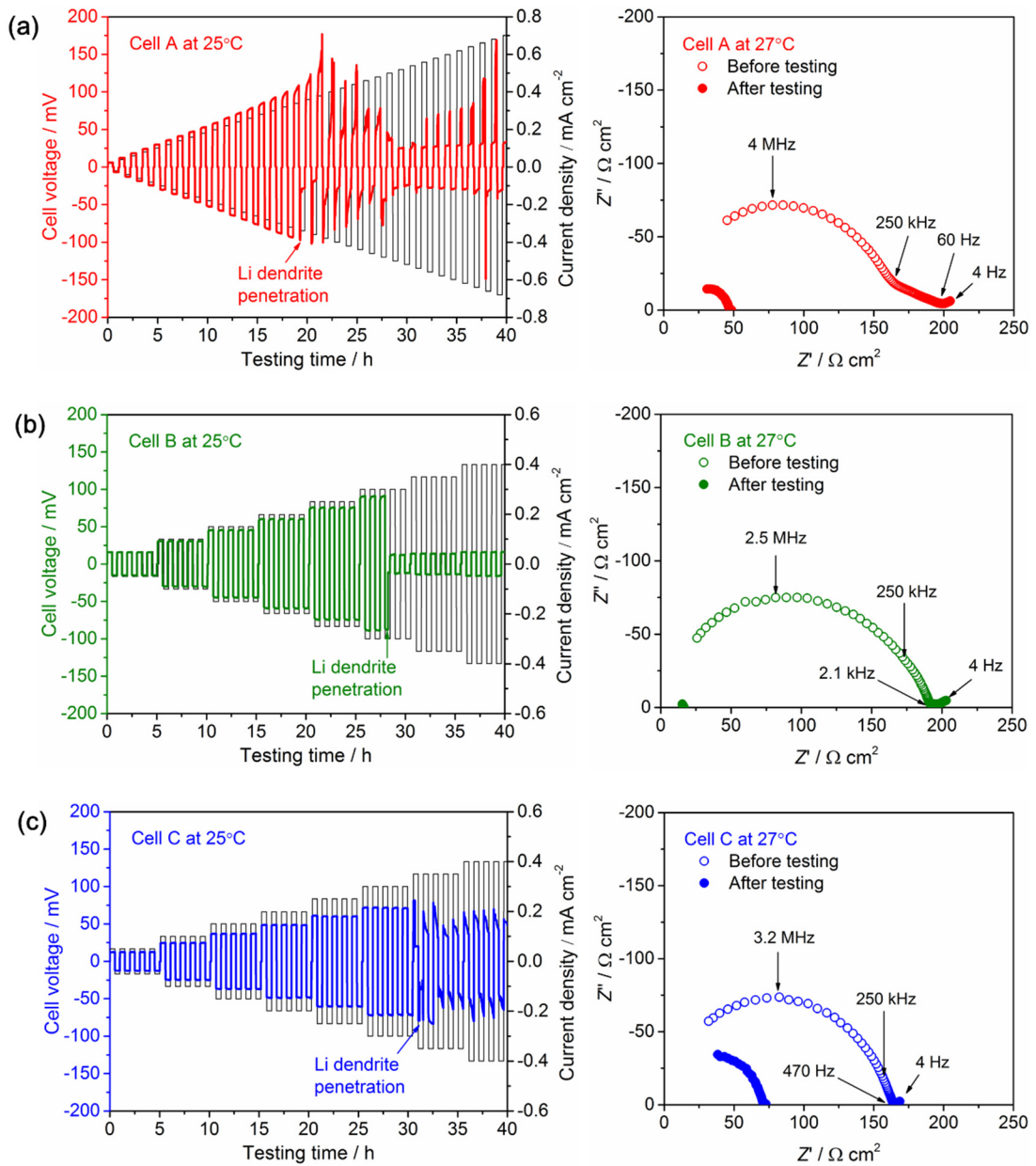
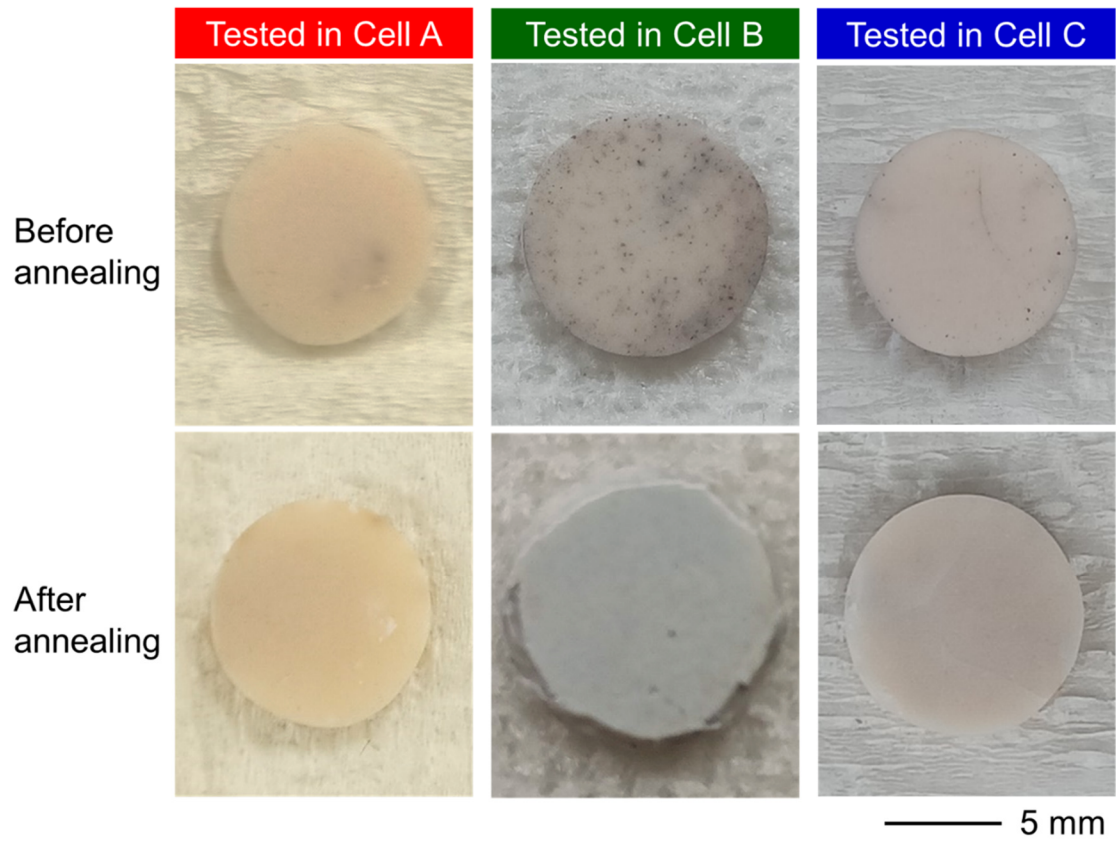


Figure 1



**Figure 2**

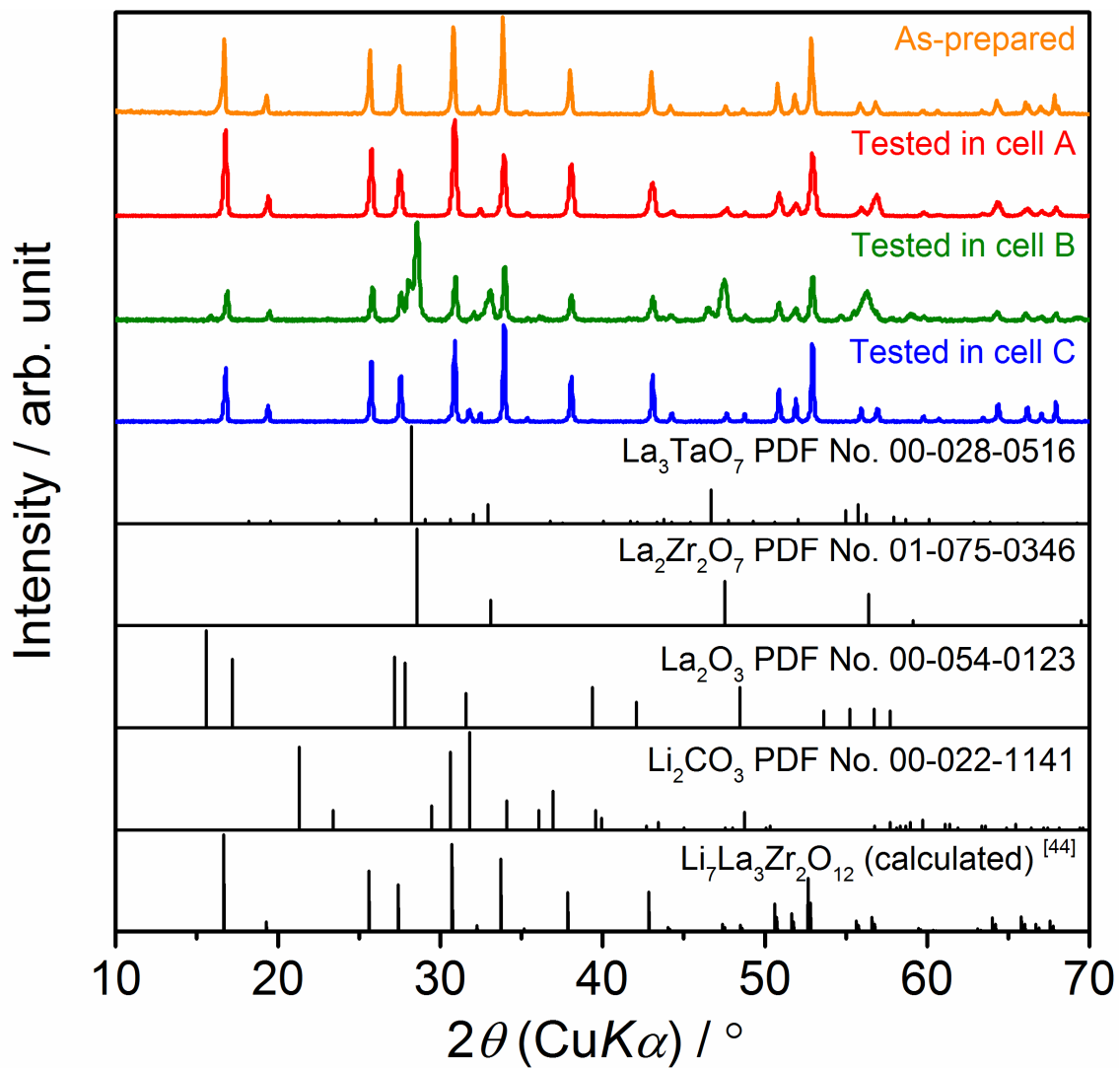


Figure 3

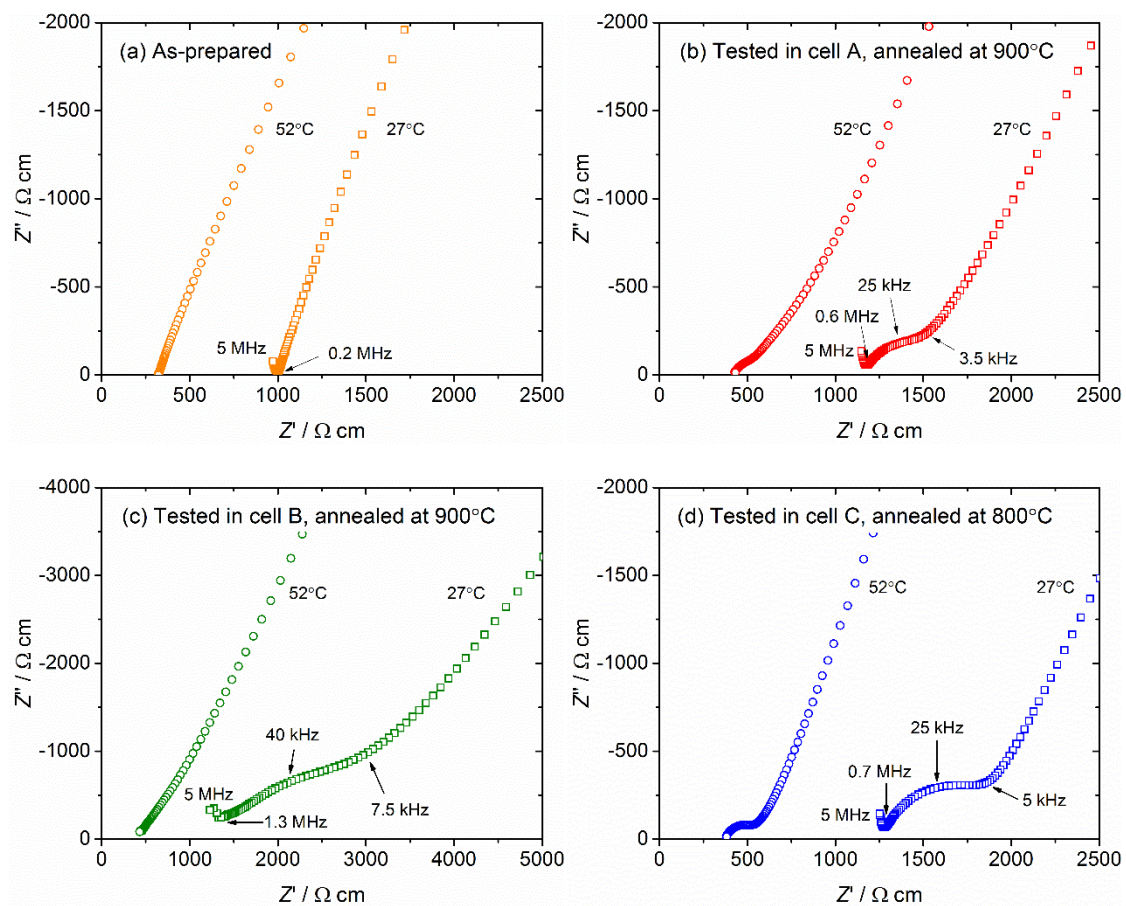


Figure 4

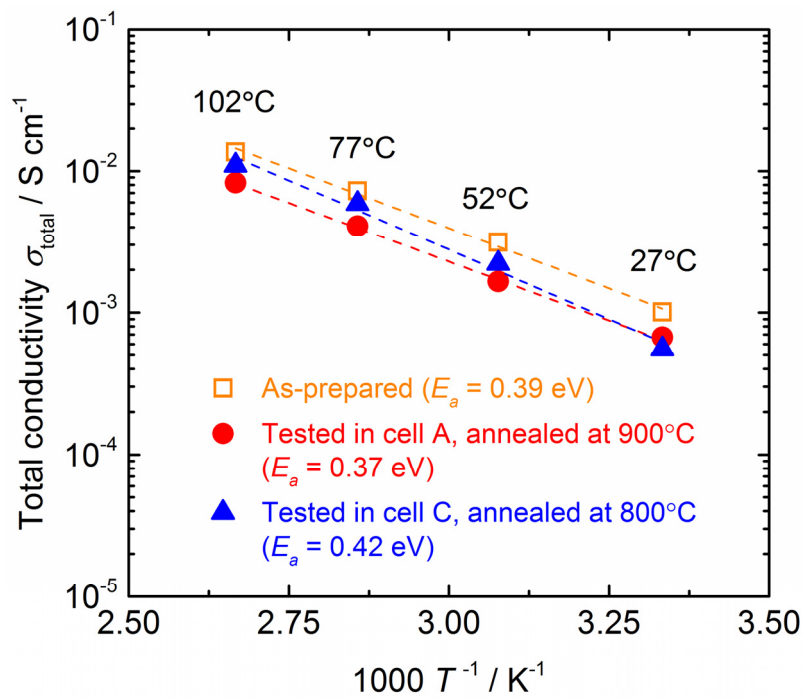


Figure 5

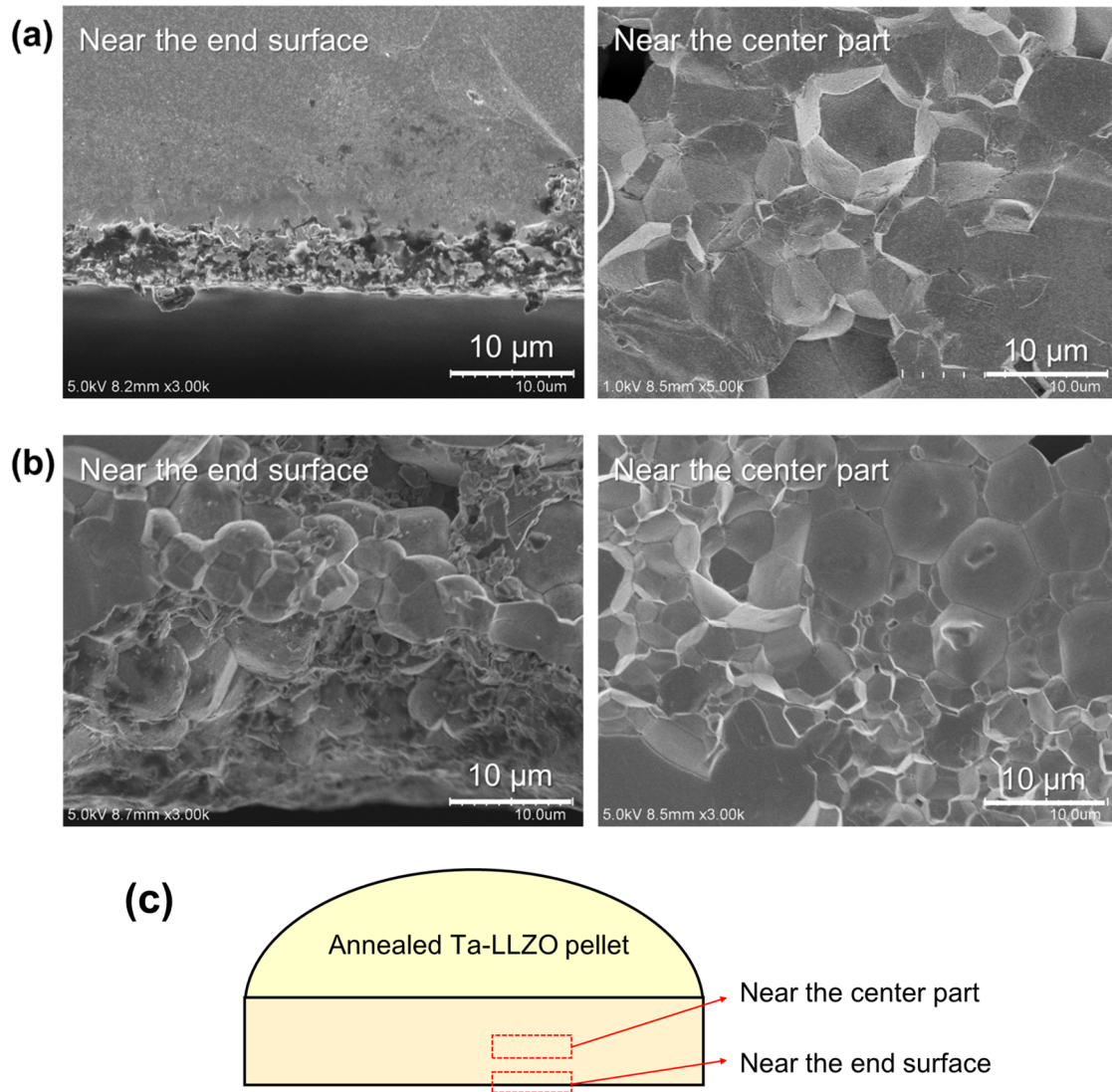


Figure 6

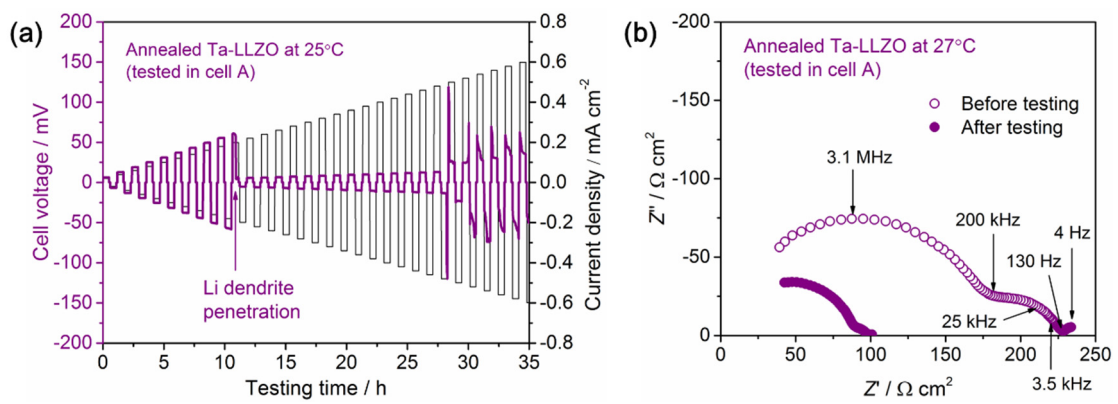


Figure 7